Qualification of uniform large area multidipolar ECR hydrogen plasma

L. Colina-Delacqua, M. Redolfi, Karim Ouaras, J. Naël-Redolfi, X. Bonnin, A. Michau, K. Hassouni, G. Lombardi

Qualification of uniform large area multidipolar ECR hydrogen plasma

Cite as: Phys. Plasmas **29**, 043508 (2022); https://doi.org/10.1063/5.0083341
Submitted: 24 December 2021 • Accepted: 13 March 2022 • Published Online: 04 April 2022

L. Colina-Delacqua, M. Redolfi, K. Ouaras, et al.

Physics of Plasmas ARTICLE scitation.org/journal/php

Qualification of uniform large area multidipolar ECR hydrogen plasma

Cite as: Phys. Plasmas **29**, 043508 (2022); doi: 10.1063/5.0083341
Submitted: 24 December 2021 · Accepted: 13 March 2022 ·
Published Online: 4 April 2022

L. Colina-Delacqua,[1] M. Redolfi,[1,a)] K. Ouaras,[1,2] J. Naël-Redolfi,[1] X. Bonnin,[3] A. Michau,[1] K. Hassouni,[1] and G. Lombardi[1]

AFFILIATIONS

[1]LSPM, CNRS-UPR3407, Université Sorbonne Paris Nord, 99 av. J. B. Clément, 93430 Villetaneuse, France
[2]LPICM, CNRS, École Polytechnique, Institut Polytechnique de Paris, 91128 Palaiseau, France
[3]ITER Organization, Route de Vinon-sur-Verdon, 13067 St-Paul-lez-Durance, France

[a)]Author to whom correspondence should be addressed: michael.redolfi@lspm.cnrs.fr

ABSTRACT

The design and characterization of a multi-dipolar microwave electron cyclotron resonance (ECR) hydrogen plasma reactor are presented. In this configuration, 16 ECR sources are disposed uniformly along the azimuthal direction at a constant distance from the center of a cylindrical reactor. Several plasma diagnostics have been used to determine key parameters such as neutral species temperature; electron density and temperature; and H^+, H_2^+, and H_3^+ ion energy distributions. The experimental characterization is supported by electromagnetic and magnetostatic field simulations as well as Particle In-Cell Monte Carlo Collisions simulations to analyze the observed ion energy distribution functions. Especially, we show that both electron density and temperature are spatially uniform, i.e., 10^{11} cm^{-3} and 3 eV, respectively. This plasma enables generating ion flux and energy in the ranges 10^{19}–10^{22} ions m^{-2} s^{-1} and few keVs, respectively. The H_2^+ ion distribution function shows two populations which were attributed to surface effects. These features make this reactor particularly suitable for studying hydrogen plasma surface interaction under controlled conditions.

I. INTRODUCTION

Scale-up and improvement of plasma systems dedicated to fundamental studies (plasma-surface interaction—PSI) and material processing (thin film deposition, etching, implantation, etc.) call for the development of large volume, uniform, and dense plasmas.[1,2] Presently, Radio-Frequency Capacitively Coupled Plasma (RF-CCP) is the most common plasma system used for uniform deposition on a large surface area (6-in. wafer). However, these discharges suffer from a relatively low plasma density (electron density around 10^9–10^{10} cm^{-3}) that may limit the process performances, such as deposition or etching rates. This motivated several groups to adopt high-frequency microwave plasma systems that provide larger, more uniform, and denser plasma (up to $\sim 10^{11}$–10^{12} cm^{-3} plasma density).[2,3] In addition to application purposes, the development of high-density plasma devices is required for investigating fundamental aspects of PSI. For example, laboratory plasmas producing strong fluxes of hydrogen ions are used to mimic conditions encountered in Scrape-off-layer (SOL) of fusion plasma devices (cold region).[4–7] This enabled investigating the interaction between high deuterium ion flux and the divertor material.[8–11] Such laboratory "PSI simulators" have already been used for carbon and tungsten material studies.[4–6,8,9,12]

Several research groups attempted to develop and characterize large area and/or volume microwave sources,[13–17] many of which made use of electron cyclotron resonance (ECR) coupling. Ono *et al.*[13] investigated high density large area argon plasmas, i.e., up to 10^{13} cm^{-3} density and 45 cm diameter, generated in plane-slotted antennas with permanent magnets. Sholze *et al.*[16] used an arrangement of several wave guides equipped with l/4 antennas to produce large area argon plasmas with a density of approximately 10^{10} cm^{-3}. Latrasse *et al.*[14] used dipolar sources similar to those used in this work and arranged in a matrix configuration to generate a planar argon plasma sheet with density as high as 10^{13} cm^{-3}. One can also mention the work done by Rayar *et al.*[15] and Tarey *et al.*[2] who used ECR sources in a square matrix configuration to generate hydrogen discharges under pressure in the range 1–100 Pa. They reported an electron density value of the order of 10^{11} cm^{-3}.

In this article, we focus on characterizing a home-made plasma system that aims at studying PSI phenomena involving carbon or

tungsten materials facing hydrogen plasma. For this purpose, a low-pressure/high density plasma system, called CASIMIR, which stands for Chemical Ablation, Sputtering, Ionization, Multi-wall Interaction, and Redeposition, has been developed. It relies on a combination of 16 ECR sources that are disposed uniformly along the azimuthal direction at a constant distance from the reactor center. Each source provides a local magnetic confinement, which results in the formation of a very high density plasma in its vicinity. The use of an arrangement of 16 sources in an azimuthal configuration makes it possible to preserve this high density produced in the vicinity of each source in the remote diffusion plasma that occupies a large region in the CASIMIR reactor (cf. Fig. 1). This configuration also enables this diffusion plasma to interact with large surface samples.

The experimental setup and the characterization tools are presented in Sec. II. Section III deals with the characterization and simulations of several aspects of the H_2 discharges, including (i) the configuration of the magneto-static and electromagnetic fields, (ii) the H_2 plasma features, i.e., electron density n_e, electron temperature T_e, rotational temperature T_{rot}, and ion distribution function, and (iii) Particle-In-Cell Monte Carlo simulation to analyze the observed ion energy distribution functions (IEDF).

II. EXPERIMENTAL SETUP AND DIAGNOSTICS TOOLS

Figure 1 shows a schematic drawing of the CASIMIR reactor. The cylindrical chamber is made of stainless steel and has a volume of ~31 (radius = 12.5 cm and height = 6 cm). The CASIMIR device is equipped with several optical ports for spectroscopic measurements. It uses 16 microwave dipolar Electron Cyclotron Resonance (ECR) sources[18,19] from *Boreal Plasma* equally distributed along the wall of the chamber. Each source consists of a coaxial waveguide that can support up to 200 W microwave power radiations. The magnetic induction needed to ensure the ECR coupling is provided by a Sm_2Co_{17} magnet located at the end section of the source. The microwave power is radiated through a small gap located between the end section of the wave guide and the magnet. The ECR sources are powered by a *SAIREM* microwave (MW) generator (2.45 GHz) GMP 30 K providing a maximum power of 3 kW. To distribute the power on the 16 sources, the applicators are connected to the power supply through a microwave power splitter. The microwaves are transmitted by a coaxial cable connected to a circulator with a water charge adapted to absorb the reflected power. The H_2 gas is injected through upper and lower home-made $^1/_4''$-diameter six-hole showerheads. The system achieves a base vacuum pressure of the order of 10^{-4} Pa, thanks to a dry (Alcatel ACPA15) and a turbo-molecular pumps (Pfeiffer, with a pumping rate of 250 l s^{-1}). Typical experiments were conducted at pressures ranging between 0.1 and 1 Pa. The pressure is monitored with a combination of Penning-Pirani (Ionivac, Leybold) and 1 mbar range capacitive gauge (Ceravac, Leybold). The flow rate ranges between 1 and 3 sccm. It is monitored by a mass flow controller (MKS) and a butterfly valve regulation system (VAT control butterfly valve). Taking the whole volume of Casimir reactor as a reference, this device delivers average volume and surface power densities of 1 W cm^{-3} and 80 W cm^{-2}, respectively. Considering the particular geometry and the very low-pressure conditions, the CASIMIR reactor tends to favor surface processes over volume ones (lower volume reactivity and large surface-to-volume ratio). As a matter of fact, the 0.1 cm^{-1} surface-to-volume ratio, in the Casimir Reactor, and the 3 cm mean free paths value estimated using a charge exchange collision cross section of 50 Å^2 for ions indicate that ions experience an average of only three gas-phase collisions before reaching the surface.

To measure the magnetic induction inside the vessel, we used a Hall Effect gauss meter (GM08 model from Hirst Magnetic Instruments). The axial and radial distributions of the magnetic induction along the magnet axis and radial directions were monitored for a

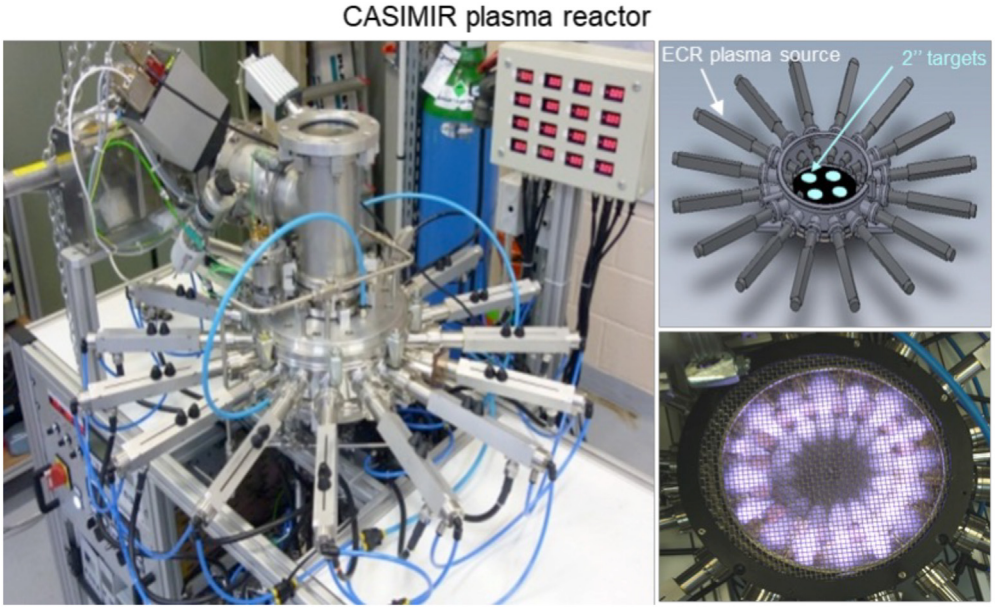

FIG. 1. Schematic representation of the CASIMIR plasma device showing the 16 ECR sources, the material target disposition, and a plasma picture.

single dipolar source on 10 cm distance starting from the end section of the magnet for the axial distribution and its lateral surface for the radial distribution. Typical absolute measurement errors in these experiments are 1 Gauss and 1 mm for the magnetic induction and the probe position, respectively.

Optical Emission Spectroscopy measurements were performed using the 1m-focal length Jobin-Yvon THR 1000 spectrometer equipped with 1800 grooves mm^{-1} grating, blazed at 450 nm, along with a R2949 Hamamatsu photomultiplier tube for the detection. The system provides a resolution of 0.0067 nm. The H_2 rotational temperature was estimated using a Boltzmann plot of the rotational distribution of the Fülcher-α ($d^3\Pi_u \rightarrow a^3\sum_g^+$) molecular hydrogen band.[20] We especially focused on the Q-branch 0–0 transition between 601 and 606.5 nm and 1–1 transition between 612 and 616.5 nm.[21] A typical rotational spectrum is shown in Fig. 2.

Hydrogen ions were analyzed using a mass spectrometer (Hiden® EQP-500). This device enables mass detection up to m/z ratio of 500. It was operated in the secondary ion mass spectrometry mode (SIMS+ and SIMS–) in order to monitor the positive and negative IEDF. In the SIMS+ mode, the MS probe was polarized between −2 and 100 V, thus enabling monitoring the IEDF over a large energy domain. It turns out that the detection of negative ions was fairly difficult. This required polarizing the probe at +200 V, which prevents any IEDF monitoring.

Electrical parameters[22] (n_e, T_e, and plasma potential V_p) were monitored radially (from the ECR source to the center of the chamber) using a cylindrical electrostatic probe from Scientific Systems® (Smartprobe). For this purpose, one of the 16 ECR sources was replaced by the probe. This change has fairly limited consequences on the diffusion plasma (where the magnetic field is no longer active), and almost no effect on the local ECR discharges generated by the other sources except the two neighboring ones. On the other hand, the diffusion plasma density depends on the ionization kinetics in the local discharges sustained by the 16 sources. Thus, the diffusion plasma density value inferred from the present measurements would be slightly lower than the value that would be obtained with 16 sources.

One of the major issues when using Langmuir probe in ECR discharges is related to the presence of the strong magnetic field, mostly around the ECR zone, that affects the electron flux to the probe and makes the classical OML theory routinely used in probe measurement no longer valid. This is especially important when the magnetic field is strong. Therefore, magnetostatic field simulations were performed in order to identify the reactor region where probe measurements interpretation with the classical OML theory is still valid.

The arrangement of the main diagnostics mentioned above is shown in Fig. 3.

III. RESULTS AND DISCUSSION

A. Electromagnetic configuration of the CASIMIR device

Prior to characterizing the H_2 plasma, a simulation of the electromagnetic configuration has been carried out. This gives useful information on the most favorable plasma ignition region and the spatial distribution of both electric and magnetic fields. Indeed, in ECR discharges, the evolution of plasma characteristics is strongly related to both spatial distribution and intensity of the magnetic induction. The static magnetic field created by the permanent magnet of the ECR source and the spatial distribution of the High-Frequency electromagnetic field radiated by the microwave source were calculated using the COMSOL® (version 3.5) software. As mentioned previously, the magnetostatic simulations are also required for assessing the plasma region where electrons are no longer magnetized, and Langmuir probe measurements based on the OML theory are still valid. The actual CASIMR electromagnetic configuration would, in principle, requires a full 3D simulation, which is out of the scope of the present work. We, therefore, proceeded in two steps. We first performed a full 3D axisymmetric simulation on the simpler single source configuration in order to obtain accurate local magnetostatic/electromagnetic configuration for each source. We then performed only 2D electromagnetic/magnetostatic simulation in order to obtain the magnetic configuration over the much larger scale of the whole CASIMIR reactor. In Subsections III A 1 and III A 2, we present the results obtained for a single source and for a set of 16 sources.

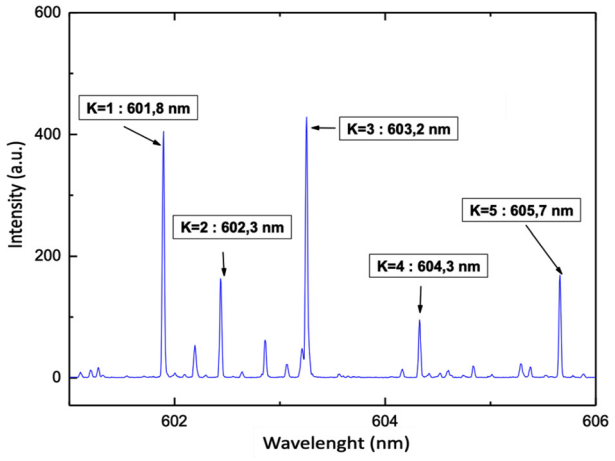

FIG. 2. Typical H_2 rotational spectrum on Q-branch 0–0 transition between 601 and 606.5 nm.

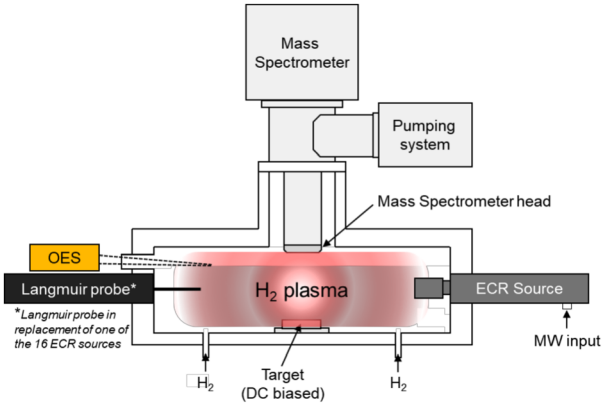

FIG. 3. Cross section schematic of the implemented diagnostics on the CASIMIR reactor device.

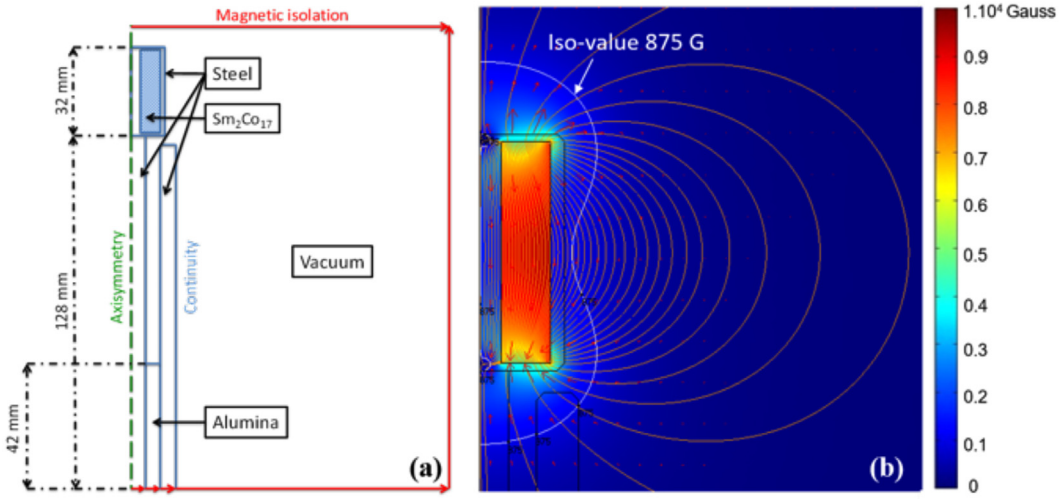

FIG. 4. (a) Schematic of the dipolar ECR source showing different magnetic domains and the boundary conditions used in the "Magnetostatics" module. (b) Mapping of magnetic flux density, magnetic field lines, and iso-value line at 875 G for a single dipolar magnet source. The top and the bottom of the magnet are set to North and South pole, respectively.

1. Static magnetic field and high-frequency electromagnetic fields generated by a single ECR source

The COMSOL® Magneto-statics module was used to simulate the topology and magnitude of the static magnetic flux generated by the Sm_2Co_{17} magnet. The dipolar ECR source, i.e., wave guide and the magnet, presents a cylindrical symmetry, and the simulation was conducted using 2-D axi-symmetry (r and z) geometry. A detailed schematic giving the geometry and the main features of the source is given in Fig. 4(a). In the magnetostatic simulations, four different zones were defined: Sm_2Co_{17} magnet, stainless steel, alumina, and vacuum. Each region of the source is considered as magnetically active through the continuity of the tangential component of the magnetic field imposed by the magnet field B_r. The walls are considered magnetically isolated (no magnetic potential at the boundaries). The remanent induction produced by the cobalt-samarium magnet and the relative magnetic permittivity-values required for determining the space distribution of the magnetic induction are given in Table I. A typical example of the simulated magnetic induction topology is shown in Fig. 4(b), where the 875 G ECR isoline is highlighted. The simulated induction is in good agreement with those measured by Hall probe-gaussmeter (see Fig. 5). Both of them decrease radially and axially and almost vanish around 3.5 cm from the magnet. This allows defining two distinct plasma regions: (i) a magnetized plasma region that extends up to 3 cm from the end section of the magnet and (ii) a non-magnetized plasma region above 3.5 cm from the magnet and up to the reactor center. The ECR zone is located at radial and axial distances of 4 and 8 mm from the magnet surface, respectively.

TABLE I. Magnetic and electrical parameters used for simulations.

Media	Relative permeability (μ_r)	Remanent magnetic field (B_r)	Electric conductivity, σ (S m^{-1})	Relative permittivity (ε_r)
Sm_2Co_{17}	1.75	1.05	1.43×10^6	⋯
Stainless steel	1.02	0	4.03×10^6	⋯
Alumina	1	0	10^{-19}	8.5
Vacuum	1	0	5.50×10^{-15}	1

The RF (sinusoid) module of COMSOL® was used to simulate the electromagnetic propagation in the coaxial waveguide and the MW radiation through the gap. Transverse Magnetic (TM) mode was selected because of the axial symmetry of the dipolar source structure.[23] The simulation domain and boundaries are shown in Fig. 6(a). We consider the metallic walls as a perfect electrical conductor. Basically, microwaves are launched at the bottom section of the wave guide denoted "entry port" in Fig. 6(a). A fraction of the input power is absorbed by the plasma, while the rest is reflected back by the perfectly metallic boundaries of the structures. The reflected wave is assumed to be fully absorbed when reaching the entry port plane. The condition of axi-symmetry is imposed along the z-axis.

The relevant input electromagnetic parameters (relative permittivity's and electrical conductivities) of both selected media are given in Table I.

The simulation results showing the electric field distribution along the coaxial waveguide are given in Fig. 6(b). We observe a harmonic wave propagation inside the coaxial waveguide with a total of four wavelengths: two short ones in alumina (zones 1 and 2) and two other longer ones in the vacuum region of the coax (zones 3 and 4). Figure 6(c) shows that the maximum electric field strength is located within the gap where the magnetic field also shows a high intensity. Therefore, the discharge is likely to ignite in this high E-field and static magnetic flux region where ionization should be enhanced and electron effectively confined. The 875 G iso-value line is fairly distant from the gap region, so effective ECR heating of the seed electrons produced

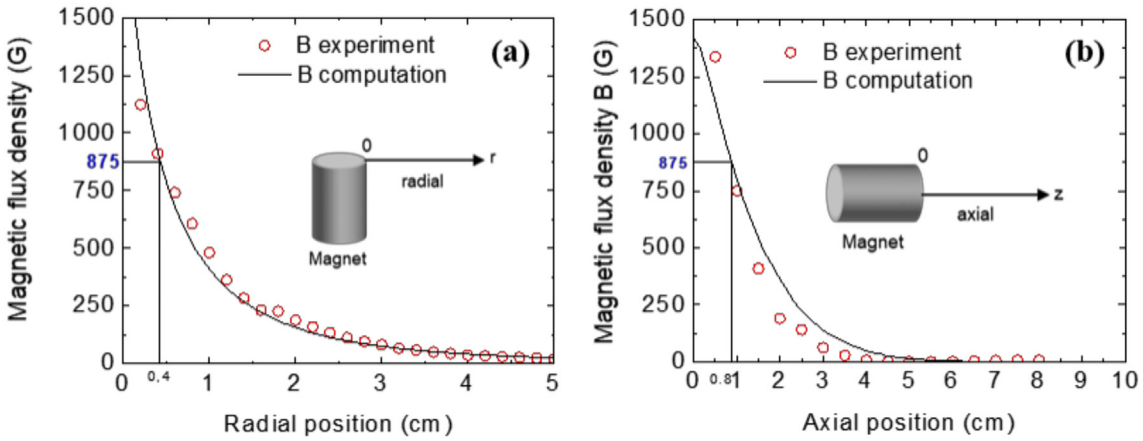

FIG. 5. Radial (a) and axial profiles (b) of magnetic flux density in the vicinity of a single magnet. (a) Position "0" is the magnet lateral surface. The distance is measured radially between the lateral surface of the magnet and the reactor center; (b) position 0 is the magnet head. The distance is measured axially between the end section of the magnet and the reactor center.

in the gap is not optimal. This effect has been also reported by Béchu *et al.*[18] Nevertheless, ECR heating does take place at a still significant E-field intensity. We should mention that the calculated electric field values do not take into account the presence of the plasma. Indeed, in the presence of a plasma, the HF field would be strongly absorbed, considering the HF penetration depth in the plasma for our typical discharge conditions, i.e., approximately 1 cm for $n_e = 10^{11}$ cm^{-3}, the wave penetration depth in the plasma would be approximately 1 cm, which is of the order of the observed plasma size. This limits the propagation of the microwaves beyond the coupling region.

2. Magnetostatic simulations of 16 and 15 dipolar ECR source combinations in CASIMIR reactor

This section deals with the simulation of the 16 and 15 ECR sources using the 2D Magnetostatics module. The dimension system is assumed infinite along the *z*-axis. The magnets have alternate polarities, which corresponds to the magnetic configuration of CASIMIR. As mentioned previously, during electrostatic probe measurements, a dipolar source was removed in order to introduce the Langmuir probe. We, therefore, performed a simulation of 15 sources in order to investigate how the magnetic topology was modified in the investigated

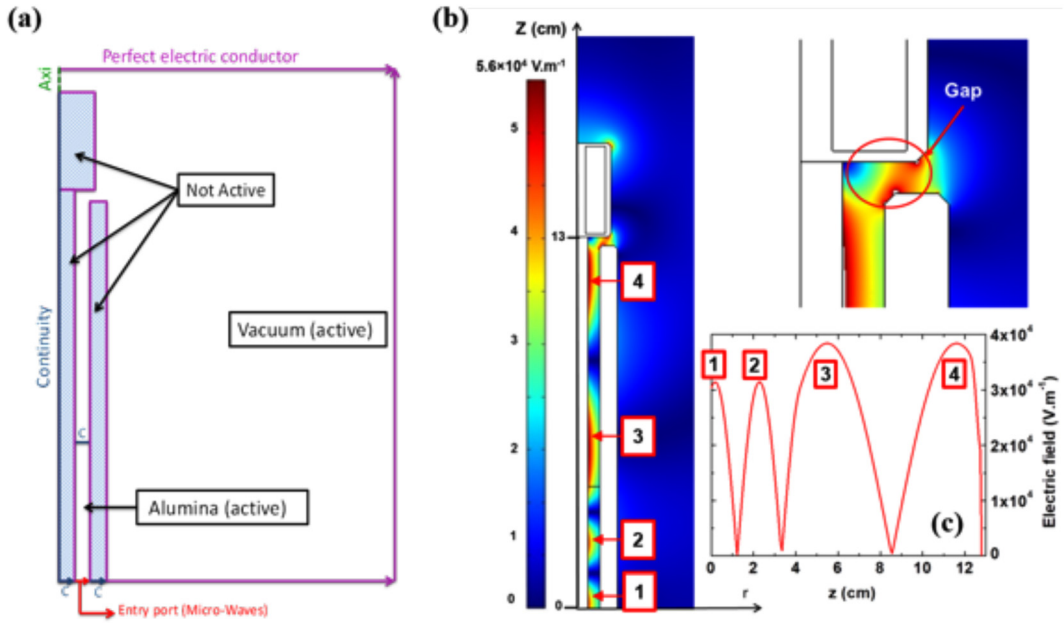

FIG. 6. (a) System considered for the "RF" module, (b) and (c) the electric field profile along the coaxial waveguide. Position corresponding to max value of E is evidenced.

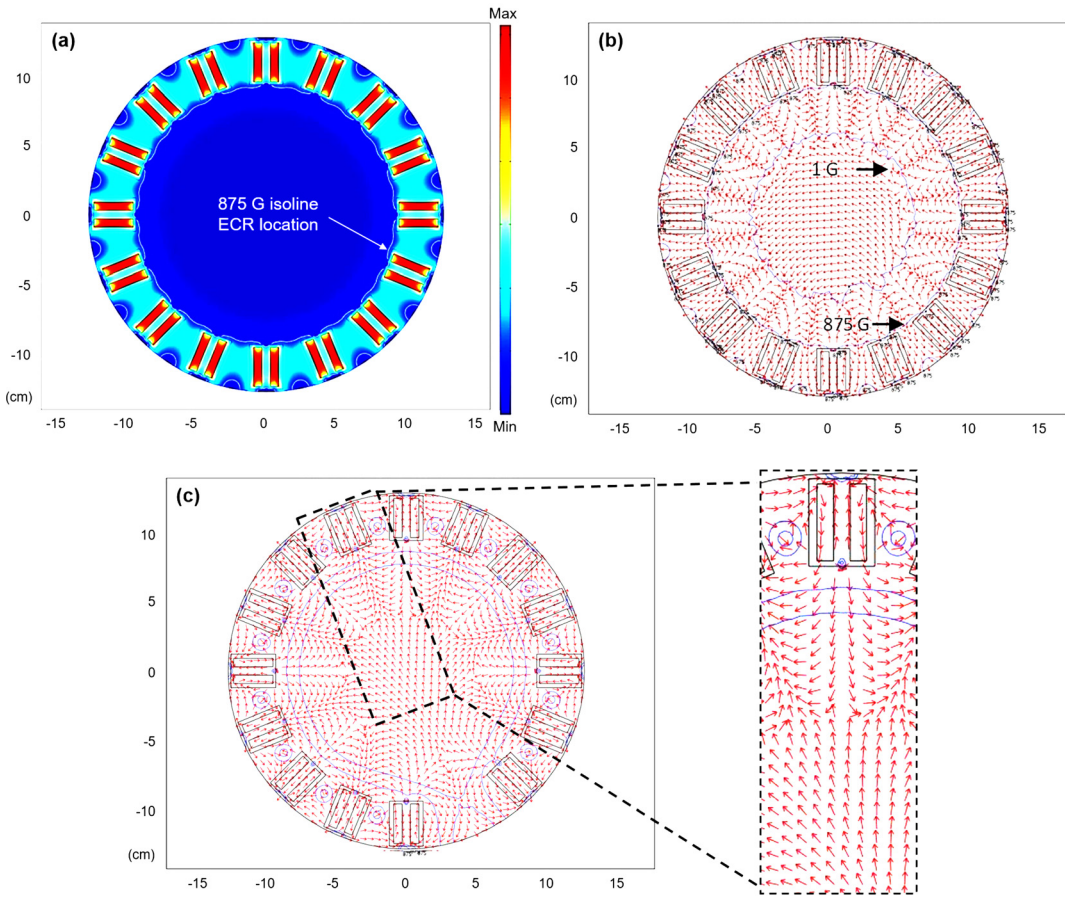

FIG. 7. (a) Mapping of the magnetic flux density, (b) field lines and iso-value lines created by 16 ECR sources with alternating polarity, and (c) field lines and iso-value lines created by 15 ECR sources with alternating polarity.

region of the reactor. The mappings of the magnetic induction strength (a) and orientation (b) of the 16 and 15 sources configuration (c) are shown in Fig. 7. The ECR region is located both in front of and between the magnets [see Figs. 7(a) and 7(b)]. As a result, the ECR line extends over all the circumference of the CASIMIR reactor at a radius value of 9 cm (see Fig. 7), thus providing an effective electron confinement in the vicinity of the magnet. The results obtained with a 16 sources configuration were compared with the magnetic induction measured using the gauss meter. Figure 8 shows good agreement between calculated and measured variations of the magnetic induction along the radial direction of the reactor. The difference between the simulations and measurements observed in the vicinity of the magnets is likely due to the fact that the simulations performed in 2D assume infinite magnets along the direction perpendicular to the plane of the simulation. The magnetic induction intensity strongly decreases beyond the circumferential ECR line (from the ECR isoline to the center).

The magnetic induction measurement enables identifying the plasma region where Langmuir measurements can be interpreted using the classical OML approach. The magnetic induction topology

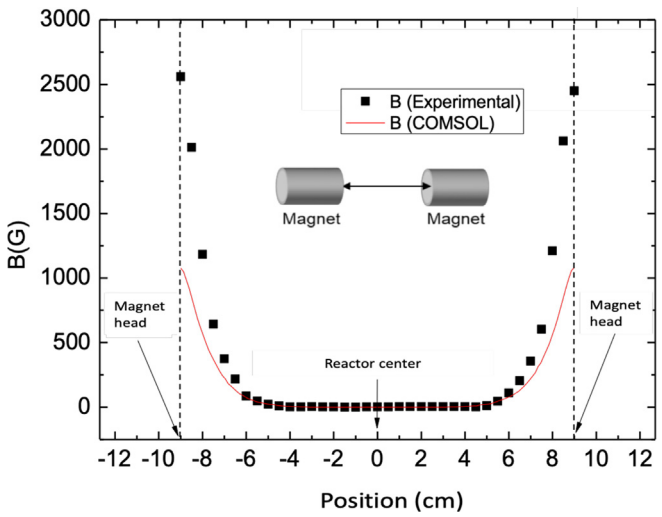

FIG. 8. Magnetic field strength profile along the reactor diameter.

used during electrostatic probe measurement, i.e., 15 dipolar sources, is shown in Fig. 7(c). Comparing 16 and 15 sources simulations, we observe that the size of central region where the magnetic induction is below 1 Gauss slightly decreases, while the magnetic field topologies in the vicinity of the dipolar source facing the probe inlet aperture are very similar for the 15 and 16 source configurations. Typically, for 2 eV electrons, the Larmor radius is of the order of the probe radius, i.e., ∼1 mm, for a magnetic induction of 50 Gauss. The electrons can be, therefore, considered as un-magnetized, for B < 50G. This value is reached at 6 and 5 cm distances from the center of the reactor when using the 16 and 15 source sets, respectively. Therefore, the whole 12 cm diameter central region of the reactor can be considered as magnetic field free during probe measurements, which enables producing uniform plasma with the 16-source system. Also, the classical OML theory can be considered as valid over little smaller plasma region, typically 10 cm diameter, when performing probe measurement with the 15-source configuration. Actually, probe measurement may be also interpreted using the classical OML theory in the magnetized region, provided the magnetic field lines are perpendicular to the collection surface of the probe so as the electrons are not magnetized along the normal to the collection surface. In order to investigate if such configuration takes place in the investigated discharge, we show the details of the magnetic flux lines in the magnetized region in the vicinity of the dipolar source. Unfortunately, the magnetic flux component parallel to the probe axis, i.e., the radial direction of CASIMIR, is very significant, and the electron flux to the collection surface should be strongly affected by the magnetic field in region with flux magnitude larger the 50 Gauss. Therefore, probe measurements can be interpreted using classical OML theory only in the diffusion plasma.

B. CASIMIR reactor characterization in pure hydrogen plasma

1. Spatial distribution of plasma parameters

Figure 9 shows the spatial evolution of the main plasma parameters, i.e., V_p, n_e, T_e, and T_{rot}, along the radial direction of the reactor (from the center to the circumferential line located at the edge of the magnets) obtained by Langmuir probe and OES measurements. Note that, as mentioned in Sec. II, probe measurements are only valid between the reactor center and the circumferential line located at 6 cm from the end sections of the dipolar sources, i.e., 0 < x < 6 cm. The values obtained outside this region are not valid (gray regions in the

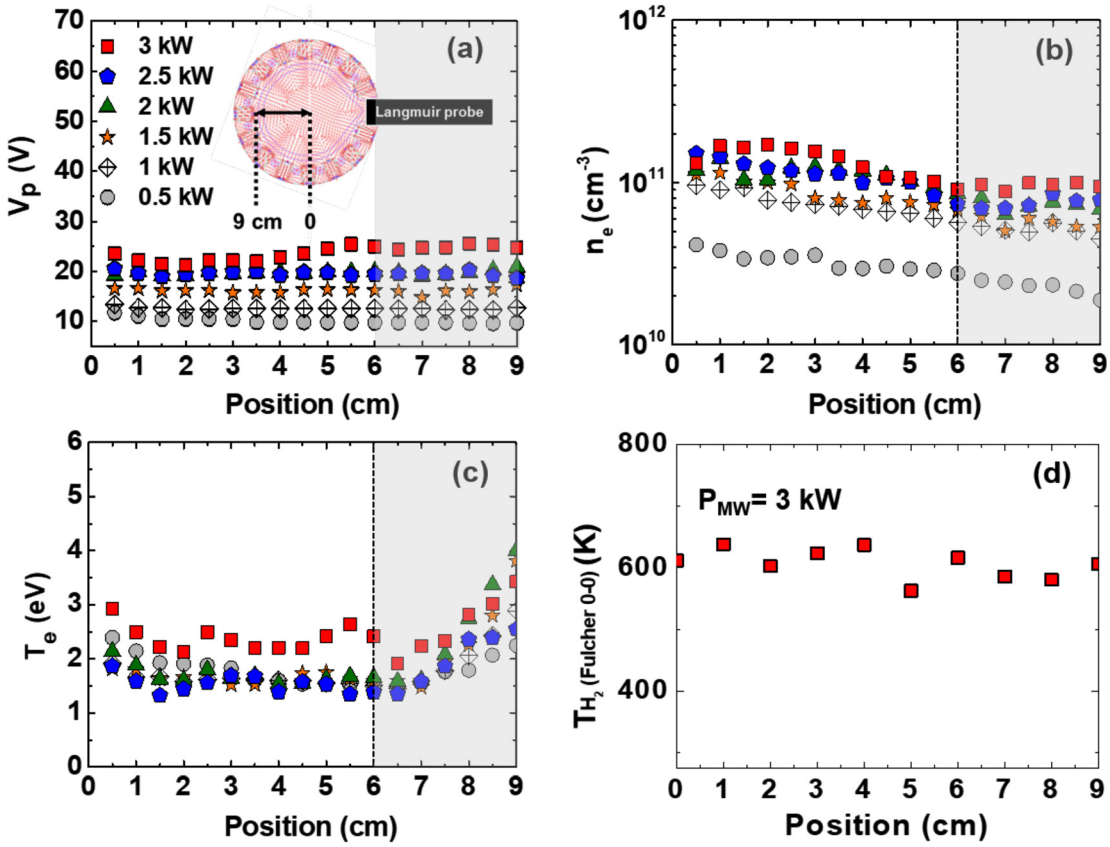

FIG. 9. Spatial distribution from the center to magnet of V_p (a), n_e (b), and T_e (c) as a function of plasma power; (d) H_2 radial rotational temperatures at 3 kW (the pressure is fixed to 0.1 Pa), the measurement error is ±50 K. The center and the magnet extremity correspond to 0 and ∼9 cm, respectively, as shown in the figure (a). The gray areas between 6 and 9 cm in figures (a)–(c) correspond to the region where the electrons are magnetized, and the OML theory is not valid. The corresponding values are just given to appreciate the trends of the plasma parameters in this region.

plots shown in Figs. 9(a)–9(c) are just given for information purpose). The radial profiles of the plasma parameters were measured at different input power values (0.5, 1, 1.5, 2, 2.5, and 3 kW). We see that n_e reaches values as high as 2×10^{11} cm^{-3} [Fig. 9(b)]. The spatial variation of n_e remains fairly moderate especially at the highest input power, for which the variation between the center and the edge of the magnet is less than 50%. One can notice that n_e is larger in the center of the reactor, even though the ionization mainly takes place in the ECR zone. This would suggest a dominant diffusion transport along the radial direction of the reactor where no magnetic confinement takes place. The magnetic confinement mainly takes place along the radial direction of the magnet in the regions between two magnets (along the azimuthal reactor direction). The electron temperature in the bulk of the plasma typically ranges between 2 and 3 eV in the investigated power range [Fig. 9(c)]. All the radial profiles of T_e show a significant increase, i.e., 1–2 eV variations, in the vicinity of the magnet. Although probe measurements are not fully valid in this region, this increase would be indicative of the ECR heating, which usually results in a non-local increase in the high-energy electron population and a subsequent increase in the observed average electron energy.

At the center of the reactor, where the plasma is quasi-neutral, $n_i = n_e$, we assume that ions are accelerated in a non-collisional sheath. Thus, the ion flux density at the entrance of the sheath is given by the product of the ion density at the sheath edge n_s and the ion Bohm velocity, i.e., $v_B = \sqrt{k_B.T_e/m_i}$, where k_B is the Boltzmann constant and m_i is the ion mass. At such low-pressure discharge conditions and low aspect ratio-plasma reactor (plasma radius is much larger than the plasma length), the ion densities at the sheath edge, n_s, and in the plasma bulk, n_0, are related by $n_s/n_0 = 0.5$.[24] This gives a typical ion flux of about 1.5×10^{20} m^{-2} s^{-1}.

Considering the sheath is assumed non-collisional, the ion energy E_{ion} is determined by taking into account the applied voltage to the sample and the plasma potential: $E_{ion} = -e.(V - V_p)$, where e is the charge of the electron, V is the applied voltage, and V_p [Fig. 9(a)].

Overall, we observe that (i) the larger the power, the larger the electron density and temperature and (ii) the electron density and temperature are almost constant along the radius of the reactor except in the vicinity of the magnet. We can, therefore, conclude that the investigated discharge system provides a uniform plasma over at least 10 cm, and probably up to 12 cm, diameter cross section. Such a system provides a uniform interaction of high-density plasmas with large substrates (up to 6 in.), which opens a large perspective for material processing applications. In addition, the plasma system investigated here is also characterized by a uniform gas temperature. This is clearly inferred from Fig. 9(d), which shows the radial profiles of the rotational temperature derived from the $d^3\Pi_u \rightarrow a^3\sum_g^+$ Fülcher system at 3 kW.[25] The rotational temperature value is about 600 K and does not vary significantly along the radius. At this condition, substrate temperature was measured by an IR pyrometer (IGA 320/23 LumaSens) in the range 500–600 K.

2. Identification of charged species and analysis of positive ion energy distribution functions

Mass spectrometry has been used to determine both the nature and the energy distributions of atomic and molecular ions that are present in the plasma. Figure 10 shows mass spectra of positive (a) and negative (b) ions obtained at 3 kW and 0.1 Pa, respectively. The main identified species are H^+, H_2^+, H_3^+, and H^-. A low density of H^- is likely to be produced at the surface of the reactor, as described in Ref. 26. Impurities such as H_2O and N_2 are also present inside the plasma at a low concentration level as may be inferred from the mass signals corresponding to several ionic species such as O^+, H_3O^+, and N_2^+.

The IEDFs observed for the three ions show quite particular features, especially for H_2^+, which exhibits a double peak [Fig. 10(c)]. The IEDF of H^+ ion is not symmetrical. The maximum energy peak value is located at 22.5 eV. We observe a slight overpopulation for the high energy part of the distribution. On the opposite, the H_3^+ ion IEDF exhibits a perfect symmetrical pattern. Its energy peak value is located at 26.5 eV. The H_2^+ IEDF is the most peculiar one since it involves two populations centered at peak-energy values of 24 and 28.5 eV, respectively. This bimodal distribution shows a minimum at an energy-value of 26.5 eV corresponding to that of H_3^+. The intensities of both peaks are of the same magnitude, which would indicate that the two H_2^+ populations (fast and slow) are comparable. The differences between these IEDFs may be due to collisional processes in the gas phase or at the surfaces. The presence of H^+ would indicate the existence of high energy electron population that favors the dissociative ionization process: $e^- + H_2 \rightarrow H^+ + H + e^-$. This is likely to take place in the ECR region.[18]

In this paper, we limit ourselves to investigate if gas phase processes can affect the ion energy distribution in the sheath between the plasma and the mass spectrometer probe. For this purpose, a Particle-In-Cell Monte Carlo Collision[27] (PIC-MCC) simulation of the electron and ion dynamics in the plasma sheath have been performed. The simulation procedure used here is similar to the one thoroughly described in Ref. 28, and only a brief description of this procedure is given here. We make use of the superparticle concept where a large number of particles of a given charged species is represented by a single superparticle. This enables reducing the number of particles that have to be tracked in the simulation. A total number of superparticles ranging between 10^6 and 10^7 were used in the present work. We follow the dynamic of each superparticle submitted to the self-consistent electric field by solving for its momentum and position using a leap-frog scheme.[28] The self-consistent field is calculated by solving Poisson's equation. The collisions between the superparticles and the neutral gas species (H_2 molecule in this case) are simulated using the null collision method. The null collision does not affect the superparticle momentum and energy. It just enables having a constant effective collision frequency and a uniformly distributed collision probability. The stochastic collision processes may be, therefore, generated using a uniformly distributed random variable. The isotropic collision process is assumed, and the change in superparticle momentum and energy during elastic or inelastic collision is treated through energy and momentum balance as described in Ref. 28.

In the simulation performed here, the plasma is assumed to be electropositive; thus, negative ions are not taken into account, and the charged species included in the simulation are H_3^+, H_2^+, H^+, and e^-. The dynamic of these four species is investigated between the free ambipolar plasma bulk and the biased target. It is worthy to mention here the difficulty that arises with a free plasma boundary in PIC/MCC simulations. As a matter of fact, an artificial numerical voltage drop appears systematically at the free boundary.[29] To avoid this spurious voltage drop, a specific voltage fitting procedure at the free

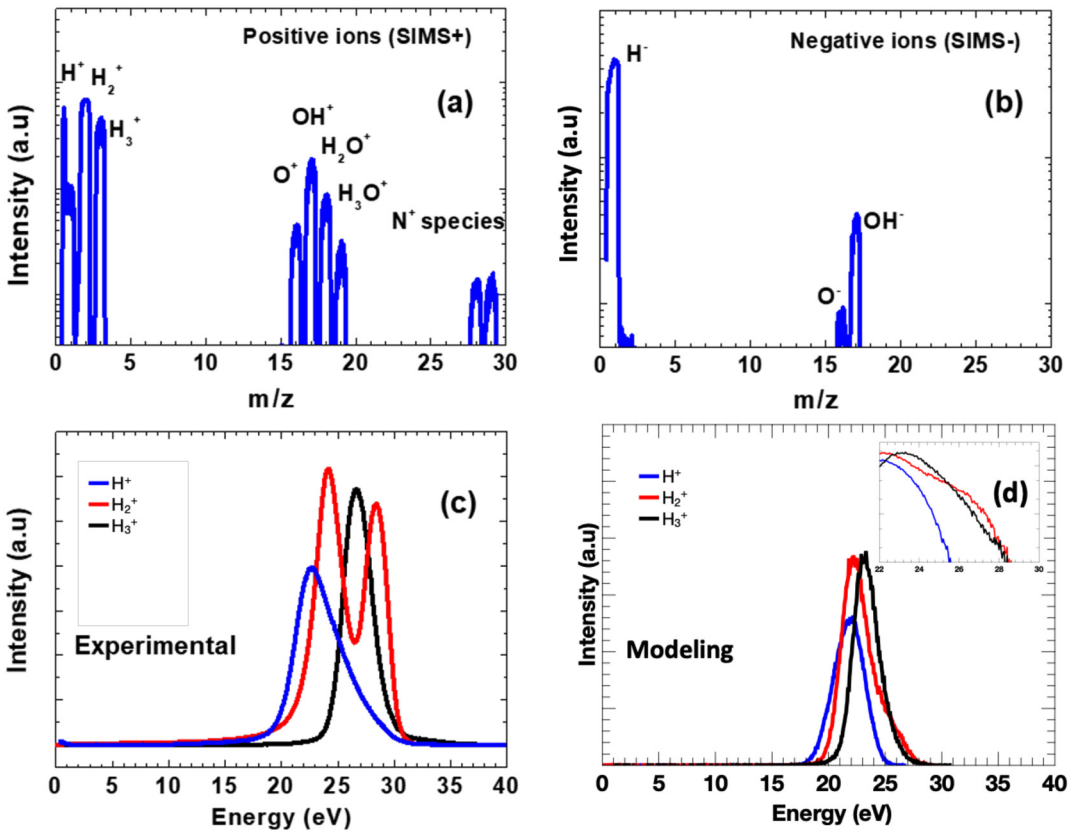

FIG. 10. Mass spectra for (a) positive ions and (b) negative ions under operating conditions and ion energy distribution of major ions species from mass spectrum measurement (c) and PIC-MCC modeling (d). For PIC-MCC simulations, we consider the following: particles number: 10^4, electron temperature: 3.5 eV, pressure: 10^{-3} mbar, and bias voltage: −10 V. Plasma conditions: 3 kW and 0.1 Pa. The inset of (d) represents the vicinity of the peaks in logarithmic scale.

boundary was proposed. This procedure is, however, difficult to apply and requires iterative approach with several PIC/MCC simulations.[29] To overcome this difficulty, we performed our simulation on a large domain that extends much beyond the sheath region and includes a large ambipolar plasma region. The voltage at the edge of the plasma region is adjusted so as to obtain the experimental value of the voltage drop in the sheath. The total ion-flux at the free ambipolar plasma boundary is obtained from the electron density and temperature measured by Langmuir probe, i.e., 10^{11} cm^{-3} and 3.5 eV, respectively. We further assume that the relative abundances of the ions at the probe surface are similar to those inferred from mass spectrometry.

The effect of collisions on both electron and ion dynamics was taken into account. The details of the processes involved in the PIC-MCC simulations are given in Table II. The cross section values used in the simulation were taken from Refs. 30–32. Specifically, electron-impact vibrational excitation (R1)–(R3), electronic excitation of molecular singlet (R4)–(R6) and triplet (R7)–(R9) states, dissociative excitation of H-atom excited states (R10) and (R11), and ionization of H_2 (R12) were taken into account in the investigation of the electron dynamics. Furthermore, in order to investigate the role of collisions in shaping the IEDFs, we took into account energy-specific charge exchange and ion conversion processes that may result in several ion populations such as those observed in the experimental mass spectrum. In particular, slow H_2^+ ions may be produced through ion conversion processes (R13), (R15), and (R18), while fast H_2^+ are obtained through reaction (R17) and fast H^+ through reaction (R16).

Figure 10(d) shows the H_3^+, H_2^+, and H^+ ions energy distribution functions calculated by the PIC-MC model for a surface bias of −10 V. Practically, this bias corresponds to the voltage applied to the mass spectrometer. Since the plasma potential is approximately 15 V, the resulting potential drop between the mass spectrometer and the plasma is around 25 V. It is worthy to mention here that the excitation of H_2 internal modes, especially the rotational and vibrational ones, by H^+–H_2 collisions was not taken into account since their cross section and energy loss function values are negligible with respect to those of H^+–H_2 elastic energy transfer (recoil).[34] We observe that all calculated IEDFs are quite symmetric. They are centered at 21, 23.5, and 24 eV for H^+, H_2^+, and H_3^+, respectively. The H^+ and H_3^+ IEDFs show a Gaussian shape with well-defined maxima. The H_2^+ IEDF shows much less symmetric shape with much slower population depletion on the high energy tail of the distribution. This may be clearly seen in the insert of Fig. 10(d) where we plotted the IEDFs around their maximum positions in a logarithmic scale. Even though our simulations yield overpopulated H_2^+ IEDFs above the peak-energy, they do not reproduce the peculiarities observed for H_2^+, i.e., a double peak distribution, in the experimental results [see Fig. 10(c)]. The larger high

TABLE II. Reaction set in the PIC-MC model.[30–34]

Collision	
$e^- + H_2\left(X^1\Sigma_g^+, v=0\right) \rightarrow e^- + H_2\left(X^1\Sigma_g^+, v=1\right)$	(R1)
$e^- + H_2\left(X^1\Sigma_g^+, v=0\right) \rightarrow e^- + H_2\left(X^1\Sigma_g^+, v=2\right)$	(R2)
$e^- + H_2\left(X^1\Sigma_g^+, v=0\right) \rightarrow e^- + H_2\left(X^1\Sigma_g^+, v=3\right)$	(R3)
$e^- + H_2\left(X^1\Sigma_g^+\right) \rightarrow e^- + H_2\left(B^1\Sigma_u^+\right)$	(R4)
$e^- + H_2\left(X^1\Sigma_g^+\right) \rightarrow e^- + H_2(C^1\Pi_u)$	(R5)
$e^- + H_2\left(X^1\Sigma_g^+\right) \rightarrow e^- + H_2\left(d^1\Sigma_g^+\right)$	(R6)
$e^- + H_2\left(X^1\Sigma_g^+\right) \rightarrow e^- + H_2\left(b^3\Sigma_u^+\right) \rightarrow e^- + 2H$	(R7)
$e^- + H_2\left(X^1\Sigma_g^+\right) \rightarrow e^- + H_2(c^3\Pi_u) \rightarrow e^- + 2H$	(R8)
$e^- + H_2\left(X^1\Sigma_g^+\right) \rightarrow e^- + H_2\left(a^3\Sigma_g^+\right)$	(R9)
$e^- + H_2\left(X^1\Sigma_g^+\right) \rightarrow e^- + H(n=1) + H(n=2)\,(\text{Lyman}\,\alpha)$	(R10)
$e^- + H_2\left(X^1\Sigma_g^+\right) \rightarrow e^- + H(n=1) + H(n=3)\,(\text{Balmer}\,\alpha)$	(R11)
$e^- + H_2\left(X^1\Sigma_g^+\right) \rightarrow e^- + H_2^+\left(X^1\Sigma_g^+\right)$	(R12)
$H^+ + H_2 \rightarrow H_{2\,slow}^+ + H(\varepsilon_{\text{th}} = 3.16\,\text{eV})$	(R13)
$H_2^+ + H_2 \rightarrow H_3^+ + H(\varepsilon_{\text{th}} = 0.10\,\text{eV})$	(R14)
$H_2^+ + H_2 \rightarrow H_{2\,slow}^+ + H_2(\varepsilon_{\text{th}} = 0.10\,\text{eV})$	(R15)
$H_2^+ + H_2 \rightarrow H^+ + H + H_2(\varepsilon_{\text{th}} = 5.62\,\text{eV})$	(R16)
$H_3^+ + H_2 \rightarrow H^+{}_{fast} + 2H_2(\varepsilon_{\text{th}} = 10.0\,\text{eV})$	(R17)
$H_3^+ + H_2 \rightarrow H_{2\,fast}^+ + 3H(\varepsilon_{\text{th}} = 17.78\,\text{eV})$	(R18)
$H_3^+ + H_2 \rightarrow H_{2\,slow}^+ + H_{2fast} + H_{fast}(\varepsilon_{\text{th}} = 17.78\,\text{eV})$	(R19)

energy population observed in the measured H^+ distribution was neither reproduced in the simulation.

A possible explanation for this discrepancy is that surface effects that were not taken into account in these simulations would eventually play a role in the ion kinetics and affect the measured IEDFs. As a matter of fact, Märk and co-workers[35,36] carried out a thorough investigation of molecular hydrogen ion conversion upon their interaction with either metal (stainless steel) or Highly Oriented Pyrolitic Graphite (HOPG) surfaces. More specifically, they analyzed the production of secondary ions upon molecular ion impact at metal or graphite surface for an impact energy ranging between 10 and 200 eV. The results obtained for these two materials were quite similar. Märk and co-workers showed that molecular ions can be readily dissociated producing H^+-ion following the endothermal processes:[35,36]

$$H_2^+ + \text{surface} \rightarrow H^+ + H + \text{surface},\ \Delta E = 2.69\,\text{eV}, \quad \text{(R20)}$$

$$H_3^+ + \text{surface} \rightarrow H^+ + H_2 + \text{surface},\ \Delta E = 4.39\,\text{eV}. \quad \text{(R21)}$$

Conversion of H_3^+ to H_2^+ is less likely since it requires 6.22 eV. Märk and co-workers also showed that the above conversion channels are significant even for an impact energy value of 30 eV, and that the ion conversion is almost total at an energy value of 60 eV for process (R20) and 80 V for process (R21). However, the secondary H^+ ions produced at the surface show a fairly small energy, i.e., approximately 1 eV, and cannot explain the high energy tail observed on H^+ IEDF in our experiment. Also interesting is the fact that the shape of the IEDF of the secondary ions, i.e., the ions reflected by the surface upon the impact of the primary ion, is very similar to the one obtained for H_2^+ in the present study. Another possible process that can explain the observed high energy tail of H^+ IEDF would be the production of H^+-ion through the impact of the fast neutral that can be readily produced by charge exchange processes (R13) and (R15) in the plasma. As a matter of fact, Voorhies *et al.*[37] showed that H^+-ions may be produced by fast H-atom impact on stainless steel and gold surfaces at energy as low as 300 eV. Unfortunately, the experiments developed by these authors did not allow evaluating this process in the energy range investigated in this work, i.e., around 20–30 eV. In addition to these surface processes, another possible explanation for the observed IEDF's would be the production of two H_2^+ populations and hot H^+ ions in the magnetized plasma region. Nevertheless, these possible explanations need to be further investigated by considering the detailed dynamics of hydrogen ions both in the magnetized plasma near the dipolar magnet region and inside the ion probing and pre-processing systems of the mass spectrometer.

IV. CONCLUSION

In this paper, we quantitatively showed that the CASIMR system made of 16 dipolar ECR sources is capable of producing a large volume of highly uniform discharges in hydrogen. This uniformity was, in particular, clearly evidenced by almost constant spatial distributions of electron density and temperature, gas temperature, and plasma potential in a very large ambipolar region that extends from the edge of the dipolar sources up to the center of the reactor. We also showed that this system provides highly ionized hydrogen plasmas, i.e., $10^{11}\,\text{cm}^{-3}$, at fairly low gas temperature. We showed that the ionization process results in the formation of the three H ions. The H^+ ion energy distribution function shows a significantly overpopulated high energy region. These peculiarities could not be explained on the basis of ion conversion and charge-exchange collisional-process when using PIC/MCC simulation of the sheath region separating the plasma bulk and the mass spectrometer probe. Possible explanations would be ion/surface interactions that would lead to the production of larger/smaller energy ion populations.

Nevertheless, our qualification shows that CASIMIR would be particularly suitable for processing full size wafers (deposition, etching, passivation, etc.). In addition, this reactor would enable investigating plasma/material interactions with a perfectly known and controlled plasma parameters, which is suitable for the study of dust and/or blister generation through plasma/surface interactions.

ACKNOWLEDGMENTS

This work was supported by Nos. ANR-09-BLAN-0070 and FR-FCM 4PWI.FR.11.05.

AUTHOR DECLARATIONS

Conflict of Interest

The authors have no conflicts to disclose.

DATA AVAILABILITY

The data that support the findings of this study are available within the article.

REFERENCES

[1]N. N. Koval, Y. F. Ivanov, I. V. Lopatin, Y. H. Akhmadeev, V. V. Shugurov, O. V. Krysina, and V. V. Denisov, Russ. J. General Chem. **85**, 1326 (2015).
[2]R. D. Tarey, A. Ganguli, D. Sahu, R. Narayanan, and N. Arora, Plasma Sources Sci. Technol. **26**, 015009 (2017).
[3]Q. Zhang, G. Zhang, S. Wang, and L. Wang, Plasma Sources Sci. Technol. **20**, 015025 (2011).
[4]A. Bock, H. Doerk, R. Fischer, D. Rittich, J. Stober, A. Burckhart, E. Fable, B. Geiger, A. Mlynek, M. Reich, H. Zohm, and A. U. Team, Phys. Plasmas **25**, 9 (2018).
[5]E. Z. Li, K. Chen, H. Liu, L. Zhang, and X. Gong, Phys. Plasmas **25**, 5 (2018).
[6]D. C. van Vugt, G. T. A. Huijsmans, M. Hoelzl, A. Loarte, A. U. Team, E. Uro, and M. Team, Phys. Plasmas **26**, 11 (2019).
[7]D. K. Kim and S. H. Hong, Phys. Plasmas **12**, 9 (2005).
[8]K. Ouaras, S. Dine, D. Vrel, X. Bonnin, M. Redolfi, G. Lombardi, and K. Hassouni, Int. J. Hydrogen Energy **39**, 17422 (2014).
[9]K. Ouaras, M. Redolfi, D. Vrel, C. Quiros, G. Lombardi, X. Bonnin, and K. Hassouni, J. Fusion Energy **37**, 144 (2018).
[10]C. Quiros, J. Mougenot, R. Bisson, M. Redolfi, A. Michau, K. Hassouni, and G. Lombardi, Nucl. Mater. Energy **20**, 5 (2019).
[11]A. Manhard, T. Schwarz-Selinger, and W. Jacob, Plasma Sources Sci. Technol. **20**, 015010 (2011).
[12]K. Ouaras, L. Colina Delacqua, C. Quirós, G. Lombardi, M. Redolfi, D. Vrel, K. Hassouni, and X. Bonnin, J. Phys.: Conf. Ser. **591**, 012029 (2015).
[13]T. Ono, S. Hiyama, Y. Nakagawa, S. Iizuka, and N. Sato, Plasma Sources Sci. Technol. **5**, 293 (1996).
[14]L. Latrasse, N. Sadeghi, A. Lacoste, A. Bes, and J. Pelletier, J. Phys. D **40**, 5177 (2007).
[15]M. Rayar, L. Quoc, A. Lacoste, L. Latrasse, and J. Pelletier, Plasma Sources Sci. Technol. **18**, 7 (2009).
[16]F. Scholze, H. Neumann, M. Zeuner, F. Bigl, and J. Mai, Surf. Coat. Technol. **97**, 755 (1997).
[17]G. J. M. Hagelaar, K. Makasheva, L. Garrigues, and J. P. Boeuf, J. Phys. D **42**, 12 (2009).
[18]S. Bechu, O. Maulat, Y. Arnal, D. Vempaire, A. Lacoste, and J. Pelletier, Surf. Coat. Technol. **186**, 170 (2004).
[19]A. Lacoste, S. Bechu, O. Maulat, J. Pelletier, and Y. Arnal, Plasma Sources Sci. Technol. **18**, 8 (2009).
[20]A. S. C. Nave, B. Baudrillart, S. Hamann, F. Benedic, G. Lombardi, A. Gicquel, J. H. van Helden, and J. Roepcke, Plasma Sources Sci. Technol. **25**, 065003 (2016).
[21]S. Brezinsek, P. Mertens, A. Pospieszczyk, G. Sergienko, and P. T. Greenland, Contrib. Plasma Phys. **42**, 668 (2002).
[22]J. G. Laframboise and L. J. Sonmor, J. Geophys. Res. **98**, 337, https://doi.org/10.1029/92JA00839 (1993).
[23]J. Margot and M. Moisan, J. Phys. D **24**, 1765 (1991).
[24]M. A. Lieberman and A. J. Lichtenberg, *Principles of Plasma Discharges and Materials Processing*, 2nd ed. (Wiley, 2005).
[25]G. L. Majstorovic, N. M. Sisovic, and N. Konjevic, Plasma Sources Sci. Technol. **16**, 750 (2007).
[26]J. P. J. Dubois, K. Achkasov, D. Kogut, A. Ahmad, J. M. Layet, A. Simonin, and G. Cartry, J. Appl. Phys. **119**, 193301 (2016).
[27]M. J. Kushner, J. Appl. Phys. **54**, 4958 (1983).
[28]S. Longo, Plasma Sources Sci. Technol. **15**, S181 (2006).
[29]G. Gozadinos, D. Vender, and M. M. Turner, J. Comput. Phys. **172**, 348 (2001).
[30]R. K. Janev, D. Reiter, and U. Samm, *Collision Processes in Low-Temperature Hydrogen Plasma* (Institut für Plasmaphysik EURATOM Association, Trilateral Euregio Cluster, December 2003); available at https://juser.fz-juelich.de/record/38224/files/Juel_4105_Reiter.pdf
[31]J. Bretagne, G. Gousset, and T. Simko, J. Phys. D **27**, 1866 (1994).
[32]T. Simko, V. Martisovits, J. Bretagne, and G. Gousset, Phys. Rev. E **56**, 5908 (1997).
[33]H. Tawara, Y. Itikawa, H. Nishimura, and M. Yoshino, J. Phys. Chem. Ref. Data **19**, 617 (1990).
[34]A. V. Phelps, J. Phys. Chem. Ref. Data **19**, 653 (1990).
[35]S. Cernusca, H. P. Winter, F. Aumayr, A. Qayyum, W. Schustereder, C. Mair, P. Scheier, and T. D. Mark, Int. J. Mass Spectrom. **223**, 21 (2003).
[36]A. Qayyum, W. Schustereder, C. Mair, W. Hess, P. Scheier, and T. D. Mark, Phys. Scr. **T103**, 29 (2003).
[37]H. G. Voorhies and T. Ohkawa, J. Nucl. Energy, Part C **8**, 555 (1966).